EUROfusion

WPEDU-PR(18) 21375

P Vallejos et al.

Effect of poloidal phasing on ICRH power absorption

Preprint of Paper to be submitted for publication in
Nuclear Fusion

This work has been carried out within the framework of the EUROfusion Consortium and has received funding from the Euratom research and training programme 2014-2018 under grant agreement No 633053. The views and opinions expressed herein do not necessarily reflect those of the European Commission.

Effect of poloidal phasing on ICRH power absorption

Authors: P. Vallejos[1], T. Jonsson[1], R. Ragona[2,3], T. Hellsten[1]

1. Dept. of Fusion Plasma Physics, School of Electrical Engineering, KTH Royal Institute of Technology, SE-100 44 Stockholm, Sweden
2. Laboratory for Plasma Physics, LPP-ERM/KMS, Bruxelles BE
3. Department of Applied Physics, Ghent University, Ghent BE

Abstract

Two ion cyclotron resonance heating (ICRH) antenna systems are planned for ITER, each having two by four poloidal triplets. The poloidal phase difference is fixed to $\Delta\theta_{pol} = \pm 90°$, which is a consequence of the use of hybrids to implement the load resilience. Since current tokamak experiments using ICRH normally operate at $\Delta\theta_{pol} = 0°$, experience from ICRH schemes with $\Delta\theta_{pol} \neq 0°$ is lacking. In this study, the effect of poloidal phasing on ICRH power absorption is studied using the novel code FEMIC, which enables detailed resolution of the plasma domain, scrape-off layer and ICRH antennas.

Simulations of the ITER antenna and the JET ITER-like antenna show that the coupled power decreases with increasing $\Delta\theta_{pol}$ as a result of increasing destructive interference. The simulations also show that the coupling is asymmetric around $\Delta\theta_{pol} = 0°$ and that the coupling for $\Delta\theta_{pol} = -90°$ is either higher or lower than $\Delta\theta_{pol} = 90°$, depending on the direction of the toroidal magnetic field. This behavior is explained by the plasma gyrotropy. Poloidal phasing also has an effect on the flux surface averaged absorbed power. For low $\Delta\theta_{pol}$ the profiles are peaked near the magnetic axis, while for high $\Delta\theta_{pol}$ the profiles are hollow. This is caused by destructive interference at the magnetic axis and is localized to $\rho_{pol} < 0.2$ for ITER and $\rho_{pol} < 0.25$ for JET-ILA.

Keywords: Poloidal phasing, ICRH, ITER, finite element method, FEMIC, destructive interference, coupling.

1. Introduction

Ion cyclotron resonance heating (ICRH) is a versatile method for heating and control of magnetically confined fusion plasmas [1-3]. The method has been successfully tested on both tokamaks and stellarators and is expected to have an important role on ITER. The main role of ICRH is to heat bulk ions in the plasma using the fast magnetosonic wave (here referred to as the fast wave). Other important applications include heating of electrons, non-inductive current drive, generation of fast ions, wall conditioning, sawtooth stabilization, and control of impurities, current and rotational profiles [1-4].

The ICRH antennas are commonly placed at the low magnetic field side of the plasma. The antennas excite radio frequency (RF) waves that in general are evanescent in the scrape-off layer (SOL) and have to tunnel through this region before coupling to fast waves at the plasma edge. The fast waves can then propagate towards the plasma core and be absorbed through various collisionless damping mechanisms, which occur when the resonance condition $\omega = n\omega_c + k_{||}v_{||}$ is fulfilled. Here ω is the antenna angular frequency, ω_c denotes the cyclotron angular frequency, $k_{||}$ the parallel wave number, $v_{||}$ the parallel velocity of the resonant particles, and n the harmonic number. Damping on the ions occurs when the fast wave crosses an ion cyclotron resonance or a harmonic of it, while electron damping occurs through transit time magnetic pumping (TTMP) and electron Landau damping (ELD). It is

envisaged that fundamental minority heating ($n = 1$) of ^{3}He and second harmonic heating ($n = 2$) of tritium ions will be one of the main auxiliary heating schemes on ITER [1,2,5].

Two identical ICRH systems are planned to be installed on ITER, where each is designed to deliver a maximum of 20 MW of RF power operating in a frequency range between 40 and 55 MHz [3,4,6-9]. Each system consists of six poloidal by four toroidal radiating straps with a Faraday screen placed in front to minimize the parallel electric field and to decrease the heat loads. The straps are combined into two by four poloidal triplets, which make the current more uniform in each strap while reducing the total number of feeding lines (see Fig. 1). The triplets can operate at a preset phase relation. Depending on the phase relation, the radiated RF waves from the triplets are superposed in the plasma, causing constructive and destructive interference patterns.

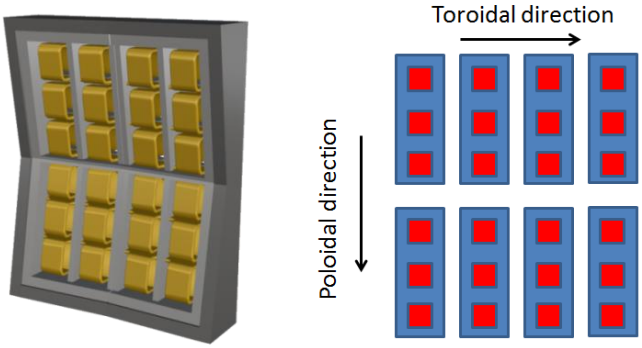

Fig 1. Left: ITER ICRH antenna. Right: Diagram of the triplet and strap configuration. Triplets are represented in blue and straps in red. The Faraday screen is not shown for clarity.

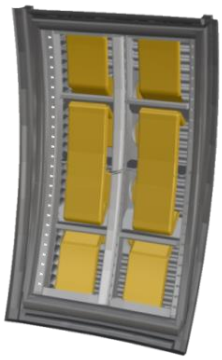

Fig 2. JET ITER like antenna (four poloidal by two toroidal antenna straps). The Faraday screen is not shown for clarity.

The phase relation in the toroidal direction (i.e. toroidal phasing) can be preset by imposing a phase difference in the sources [7,8]. This makes it possible to control the launched toroidal mode spectrum. For instance, a symmetric mode spectrum is beneficial for pure plasma heating[10], while co- and counter current drive require an asymmetric mode spectrum [11-13].

The choice of phase relation in the poloidal direction (i.e. poloidal phasing) will be restricted on ITER. This is a consequence of the use of hybrids to implement load resilience that sets the poloidal phase difference to $\Delta\theta_{pol} = \pm 90°$ between the lower and upper triplets [7-9]. Present tokamak experiment using ICRH normally operate at $\Delta\theta_{pol} = 0°$, hence experience with $\Delta\theta_{pol} \neq 0°$ is lacking. Simulations using the ANTITER [8] and TOPICA [14] codes of the ITER ICRH system have been performed for $\Delta\theta_{pol} = [0°, \pm 90°, 180°]$ [8]. They found that the highest and lowest power coupling was obtained for $\Delta\theta_{pol} = 0°$ and

$\Delta\theta_{pol} = 180°$, respectively. Their results also showed that the coupling for $\Delta\theta_{pol} = -90°$ was higher than for $\Delta\theta_{pol} = 90°$. This is explained by the fact that the coupling was asymmetric around $\Delta\theta_{pol} = 0°$. A scan in the poloidal phase difference for several toroidal phasing schemes using both TOPICA and ANTITER show that the optimal coupling occurs near $\Delta\theta_{pol} = -30°$. Among present tokamak experiments, the JET ITER like antenna (ILA) could be a suitable candidate for studying the effect of poloidal phasing. The ILA has two toroidal by four poloidal straps (see Fig. 2) and can operate at a poloidal phase difference between -90^o and 90^o [15].

In this paper, the effect of poloidal phasing on the coupling and ICRH power absorption profiles has been studied theoretically using the FEMIC (Finite Element Model for ICRH) code. In particular, the poloidal schemes $\Delta\theta_{pol} = \pm 90°$ on ITER have been evaluated with respect to performance and compared with $\Delta\theta_{pol} = 0°$, which is expected to have the best performance. A similar study was conducted on JET-ILA. Modeling these effects put some requirement on the model. More precisely, to model the effect of poloidal phasing each poloidal antenna strap must be represented as a separate geometric entity in order to apply individual boundary conditions (e.g. current amplitude and phase). In addition, to calculate the coupling and ICRH power deposition the hot dielectric tensor is required in order to have absorption by individual ion species and electrons. We focused on schemes with strong single pass damping and avoided the mode conversion regime. On ITER and JET we used a DT plasma with a small concentration of ^{3}He and a D plasma with a small concentration of H, respectively.

This paper is organized as follows. The physics and dielectric tensor is described in section 2. The FEMIC code is described in section 3. Simulation results for ITER and JET are presented in sections 4 and 5, respectively. The results are discussed in section 6 and section 7 contains the conclusions.

2. The wave equation and dielectric tensor

In this section we describe the wave equation and the dielectric tensor model. We will separate the geometry into a plasma and a SOL domain (including the antenna region). The hot dielectric tensor is applied to the plasma domain, while a simplified dielectric tensor is applied to the SOL domain.

2.1 The wave equation

In this study we use a quasi-homogeneous approximation of the dielectric tensor requiring that the parallel and perpendicular wave numbers are known in advance. We assume the geometry and the dielectric tensor to be invariant in the toroidal direction. Hence, we Fourier decompose in the toroidal direction and calculate the wave field for a single toroidal mode number, while the perpendicular wave number is given from the local fast wave dispersion relation. Under these assumptions, the wave equation reduces to 2D axisymmetry and is given by [16,17]

$$\nabla \times \nabla \times \mathbf{E} - \frac{\omega^2}{c^2}\mathbf{K}(\mathbf{r}, \mathbf{k}_\perp, k_{||})\mathbf{E} = i\omega\mu_0 \mathbf{J}_{ext}, \qquad (1)$$

where $\mathbf{K}$ is the hot dielectric tensor for a Maxwellian plasma, $\mathbf{k}_\perp$ is the perpendicular wave number, $k_{||}$ is the parallel wave number and $\mathbf{J}_{ext}$ is an external current density. Using a cylindrical coordinate system with (R, ϕ, Z), the solution has the form

$$\mathbf{E}(R, \phi, Z) = \hat{\mathbf{E}}(R, Z)e^{in_\phi \phi}, \qquad (2)$$

where $\hat{\mathbf{E}}$ is a complex amplitude and n_ϕ is the azimuthal toroidal mode number.

2.2 The plasma dielectric tensor

In a Cartesian coordinate system (x, y, z) where the magnetic field is aligned along the positive z direction and the wave vector is in the xz plane, the dielectric tensor for a hot bi-Maxwellian plasma is given by [16,17]

$$\mathbf{K}^{Stix} = \begin{bmatrix} K_1 & K_2 & K_4 \\ -K_2 & K_1 + K_0 & -K_5 \\ K_4 & K_5 & K_3 \end{bmatrix}, \qquad (3)$$

where

$$K_0 = 2\sum_j \frac{\omega_{p,j}^2 e^{-\lambda_j}}{\omega k_{||} v_{||,j}} \sum_{-\infty}^{\infty} \lambda_j (I_n - I_n') A_{n,j},$$

$$K_1 = 1 + \sum_j \frac{\omega_{p,j}^2 e^{-\lambda_j}}{\omega k_{||} v_{||,j}} \sum_{-\infty}^{\infty} \frac{n^2 I_n}{\lambda_j} A_{n,j},$$

$$K_2 = i\sum_j \frac{\epsilon_j \omega_{p,j}^2 e^{-\lambda_j}}{\omega k_{||} v_{||,j}} \sum_{-\infty}^{\infty} n (I_n - I_n') A_{n,j},$$

$$K_3 = 1 - \sum_j \frac{\omega_{p,j}^2 e^{-\lambda_j}}{\omega k_{||} v_{||,j}} \sum_{-\infty}^{\infty} I_n \left(\frac{\omega - n\omega_{c,j}}{k_{||} v_{||,j}}\right) B_{n,j},$$

$$K_4 = \sum_j \frac{k_\perp \omega_{p,j}^2 e^{-\lambda_j}}{k_{||} \omega \omega_{c,j}} \sum_{-\infty}^{\infty} \frac{n I_n}{\lambda_j} C_{n,j},$$

$$K_5 = i\sum_j \frac{k_\perp \epsilon_j \omega_{p,j}^2 e^{-\lambda_j}}{k_{||} \omega \omega_{c,j}} \sum_{-\infty}^{\infty} (I_n - I_n{}') \, C_{n,j},$$

$$A_{n,j} = \left[\left(1 - \frac{k_{||} v_{0,j}}{\omega}\right) Z(\zeta_{n,j}) + \frac{k_{||} v_{||,j}}{\omega}\left(1 - \frac{T_{\perp,j}}{T_{||,j}}\right)\frac{Z'(\zeta_{n,j})}{2}\right],$$

$$B_{n,j} = \left[\left(1 + \frac{n\omega_{c,j}}{\omega}\left(1 - \frac{T_{||,j}}{T_{\perp,j}}\right)\right) Z'(\zeta_{n,j}) + \frac{2n\omega_{c,j} T_{||,j} v_{0,j}}{\omega T_{\perp,j} v_{||,j}}\left(Z(\zeta_{n,j}) + \frac{k_{||} v_{||,j}}{\omega + n\omega_{c,j}}\right)\right],$$

$$C_{n,j} = \left[\frac{n\omega_{c,j} v_{0,j}}{\omega v_{||,j}} Z(\zeta_{n,j}) + \left(\frac{T_{\perp,j}}{T_{||,j}} - \frac{n\omega_{c,j}}{\omega}\left(1 - \frac{T_{\perp,j}}{T_{||,j}}\right)\right)\frac{Z'(\zeta_{n,j})}{2}\right].$$

Here n refers to the harmonic and j to the species numbers, $\omega_{p,j}$ is the plasma angular frequency, $\omega_{c,j}$ the cyclotron angular frequency, $\lambda_j = 0.5 k_\perp^2 \rho_{L,j}^2$ the FLR parameter, $\rho_{L,j} = v_{\perp,j}/\omega_{c,j}$ the Larmor radius, $v_{\perp,j}$ the perpendicular thermal velocity, $v_{||,j}$ the parallel thermal velocity, $v_{0,j}$ the net parallel flow velocity, $I_n = I_n(\lambda_j)$ the modified Bessel functions of order n, $T_{\perp,j}$ and $T_{||,j}$ the perpendicular and parallel temperatures, respectively, $Z(\zeta_{n,j})$ the plasma dispersion function evaluated at $\zeta_{n,j} = (\omega + n\omega_{c,j} - k_{||} v_{0,j})/(k_{||} v_{||,j})$, $\epsilon_j = q_j/|q_j|$ the charge sign and q_j the species charge.

The derivation of Eq. (3) uses a coordinate system based on the direction of the magnetic field and the wave vector. To use this tensor in a cylindrical coordinate system the dielectric tensor has to be transformed,

$$\mathbf{K} = \mathbf{R} \cdot \mathbf{K}^{Stix} \cdot \mathbf{R}^{-1}, \qquad (4)$$

where the three column vectors of the orthogonal rotation matrix $\mathbf{R}$ are given by $\boldsymbol{\kappa}$, $\mathbf{b} \times \boldsymbol{\kappa}$ and $\mathbf{b}$, for $\mathbf{b} = \mathbf{B}/|\mathbf{B}|$ and $\boldsymbol{\kappa} = \mathbf{k}_\perp/|\mathbf{k}_\perp|$. In this work the toroidal magnetic field is in the negative

ϕ direction (poloidal field neglected) and the perpendicular wave vector in the positive R direction, resulting in a transformation matrix

$$\mathbf{R} = \begin{bmatrix} 1 & 0 & 0 \\ 0 & 0 & -1 \\ 0 & 1 & 0 \end{bmatrix}. \qquad (5)$$

By using the assumptions above, the parallel and perpendicular wave numbers are given by

$$k_{||} = \frac{n_\phi}{R}, \qquad (6)$$

$$k_\perp^2 \approx \frac{\omega^2}{c^2}\left[K_1 - n_{||}^2 - \frac{K_2^2}{K_1 - n_{||}^2}\right]_{\lambda=0}, \qquad (7)$$

where $n_{||} = ck_{||}/\omega$ is the parallel component of the refractive index. Since the poloidal field is neglected, the up- and downshift in $k_{||}$ is absent. Here, $k_\perp^2$ is given by the fast wave dispersion relation (ignoring the parallel electric field and FLR effects).

The local absorption from the individual species is given by

$$Q_j = -i\omega\epsilon_0 \mathbf{E}^* \boldsymbol{\chi}_j^A \mathbf{E}, \qquad (8)$$

where $\boldsymbol{\chi}_j^A$ is the anti-Hermitian part of the susceptibility tensor $\boldsymbol{\chi}_j$ for species j.

2.3 The SOL dielectric tensor

In principle, one could use the full hot dielectric tensor in the SOL and antenna regions. However, at low temperatures the resonances become spatially thin and are challenging to resolve numerically. In contrast, a vacuum approximation is not adequate to fully describe the wave properties of the SOL. A non-zero plasma density can cause anisotropic effects, wave propagation and power losses in the SOL [18]. In addition, a non-zero plasma density in front of the antenna can improve the coupling [19], since it weakens the evanescence region and moves the fast wave cutoff density closer to the antenna (e.g. when plasma refueling is located close to the antenna). To model wave phenomena in the SOL and perform coupling studies, we propose the following generic user defined dielectric response in the SOL,

$$\mathbf{K}^{SOL} = \begin{bmatrix} \epsilon_{xx} & \epsilon_{xy} & 0 \\ \epsilon_{yx} & \epsilon_{yy} & 0 \\ 0 & 0 & \epsilon_{zz} \end{bmatrix}. \qquad (9)$$

This formulation supports a spectrum of SOL response models, ranging from vacuum to a cold plasma response with collisions.

3. The FEMIC code

The finite element method (FEM) is a robust numerical tool for solving partial differential equations that can be applied on complex geometries. The disadvantage of FEM is the difficulty of correctly accounting for spatial dispersion effects. Fourier spectral methods can handle spatial dispersion effects but have the disadvantage of producing dense matrices that are time consuming to invert. Handling complex geometries using this method is difficult and is therefore not suitable for calculations outside the plasma domain.

Several codes have been developed to model the wave fields generated by ICRH antennas that are based on FEM, Fourier spectral methods or a combination of both [20-26]. Current

modeling codes normally have a sophisticated representation of the plasma, but use a simple geometric representation of the SOL and ICRH antennas. On the other hand, codes such as TOPICA [14] and ANTITER [8] use an advanced geometric model of the ICRH antennas, but use a simplified model of the plasma core. Currently, a new method is being developed, HISTORIC, that use a FEM representation in the SOL and antenna regions and TORIC for the core plasma domain [27]. Thus, the code allows using a complex geometry in the SOL while having an accurate plasma model.

In this paper, we propose an alternative approach to model the wave fields based on FEM. Since FEM has difficulties implementing spatial dispersion effects, we use an algebraic quasi-homogeneous approximation of the dielectric tensor and evaluate finite Larmor radius (FLR) effects using the fast wave dispersion relation. This recipe is useful for cases where mode conversion to other waves is insignificant. Since the coupling is dependent on the SOL plasma density, the location of the fast wave cutoff and on the gradient of the plasma density at the cutoff [9], we propose to calculate the dielectric response beyond the separatrix (and include the plasma density gradient outside the separatrix). For these purposes, the code FEMIC (Finite Element Model for ICRH) has been developed.

3.1 Overview of FEMIC

The FEMIC code is based on two scientific programs: MATLAB® [28] and COMSOL Multiphysics® [29], including the RF Module and LiveLink™ for MATLAB®. A flow chart of the code is shown in Fig. 3.

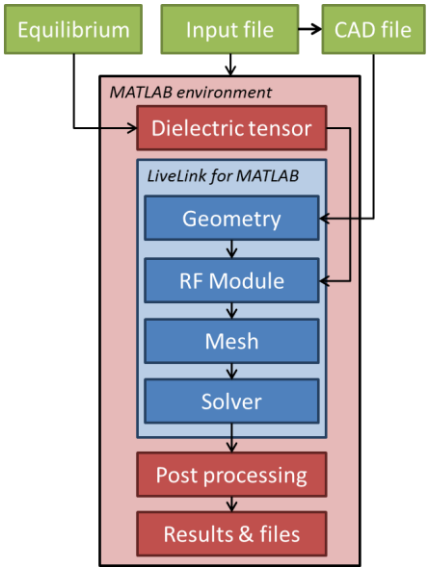

Fig 3. Flow chart of the FEMIC code. Green boxes represent input files, red boxed are MATLAB® processes and blue boxes are processes in the LiveLink™ for MATLAB®.

The FEMIC code requires three types of input files. The equilibrium input file contains the magnetic flux function ψ, the separatrix geometry and magnetic axis coordinate. The second file is the "Input file". Here, the user can specify the antenna parameters, the temperature and density profiles, the plasma species, and the numerical parameters. The third input contains the CAD geometry, which is commonly a COMSOL® file.

When executing the FEMIC code, the dielectric tensor (Eq. (3)) is calculated in MATLAB® and saved to file. MATLAB® then creates a COMSOL® model using the LiveLink™ for MATLAB®, where the following steps are performed

- Import of the 2D axisymmetric CAD geometry in the poloidal plane (see Fig. 4).

- Import of the dielectric tensor components. The dielectric tensor can then be defined in the RF Module and the wave equation is configured for one toroidal mode number. Boundary conditions are applied to the walls and the antenna boundaries.
- An unstructured triangular mesh using second order vector elements is applied on all domains (linear and cubic elements are available). The advantage of applying an unstructured mesh is that local refinement is possible, e.g. around ion cyclotron resonances and mode conversion layers. A boundary layer mesh is applied adjacent to the separatrix in order to resolve gradients in the temperature and density (see Fig. 5).
- The COMSOL® built-in direct solver MUMPS is used to solve the system of equations. The solver supports and benefits from multi-core capabilities.

Once the solution has converged, the FEM model is returned to the MATLAB® environment for post-processing, where various output results are calculated. The COMSOL® model and calculated data are saved to file.

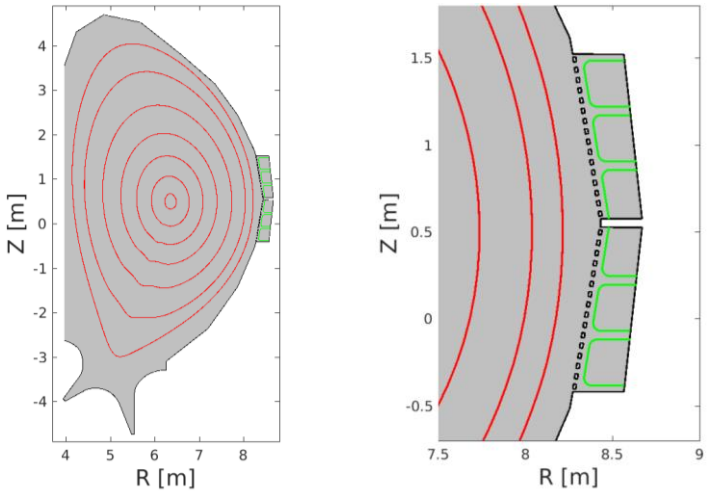

Fig. 4: Left: 2D geometry of ITER. The computational domain is shown in gray, ICRH antennas in green and magnetic flux surfaces in red. Right: Zoomed in figure showing the poloidal antennas and Faraday screen.

3.2 The geometry and boundary conditions

The geometry of ITER in the poloidal plane is shown in Fig. 4. This geometry includes an accurate representation of the first wall, divertor and antenna regions, including all six poloidal antenna straps and the Faraday screen. The first wall and Faraday screen are assumed to be perfect conductors with no losses. Thus, the boundary condition $\hat{\mathbf{n}} \times \mathbf{E} = \mathbf{0}$ is applied, where $\hat{\mathbf{n}}$ is a unit normal vector. The antenna straps are represented as internal boundaries. If we denote the antenna from top to bottom using the subscript $k = 1,2,3,4,5,6$, the current density condition is given by

$$\mathbf{J}_k = \mathbf{t}_{ant} \tilde{J}_k e^{i\theta_k}, \qquad (10)$$

where $\mathbf{t}_{ant}$ is the unit tangential vector in the poloidal plane of the antenna boundary, $\tilde{J}_k$ the current density amplitude and θ_k the phase. To operate at a poloidal phase difference of $\Delta\theta_{pol} = 0°$ means that all six poloidal antennas are operating at the same phase, i.e. $\theta_k = \hat{\theta}$ for all k where $\hat{\theta}$ is a constant. To operate at $\Delta\theta_{pol} = \pm 90°$, we apply $\theta_{1,2,3} = \hat{\theta}$ on the upper triplet and $\theta_{4,5,6} = \hat{\theta} \pm 90°$ on the lower triplet. This works similar for JET-ILA, but using four poloidal antennas.

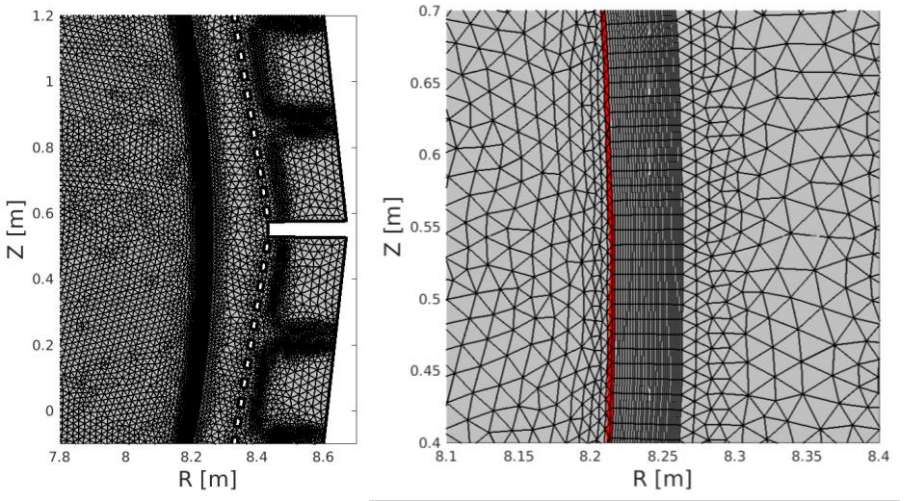

Fig 5: Left: Example of a mesh on the ITER geometry near the antenna region. Right: Zoomed in figure showing the boundary layer mesh on the plasma domain boundary. The red line is the separatrix.

3.3 Magnetic flux surfaces

The magnetic equilibrium used in this study for ITER is illustrated in Fig. 4 using red solid lines, where the outermost red line corresponds to the separatrix. The flux surfaces in the FEMIC code are used to define the temperature and density profiles as well as the internal boundary that separates the plasma and SOL domains. These are defined by using the magnetic flux function $\psi = \psi(R, Z)$ that can be defined either by analytical expressions or from file. Here, we use the flux label ρ_{pol} to identify a specific flux surface, which is given by

$$\rho_{pol} = \begin{cases} \left(\frac{\psi-\psi_{axis}}{\psi_{sep}-\psi_{axis}}\right)^{1/2}, & \{R,Z\} \ \ inside\ separatrix \\ \left(1+\left|\frac{\psi-\psi_{axis}}{\psi_{sep}-\psi_{axis}}\right|\right)^{1/2}, & \{R,Z\} \ outside\ separatrix \end{cases} \tag{11}$$

where ψ_{axis} and ψ_{sep} are the flux function values on the magnetic axis and separatrix, respectively.

3.4 Magnetic field, density and temperature profiles

The toroidal magnetic field strength in this study is given by a vacuum approximation

$$B = \frac{B_0 R_0}{R}, \tag{12}$$

where B_0 is the on-axis magnetic field and R_0 the corresponding R-coordinate. The temperature and density profiles are described by analytical expressions, given by

$$g(\rho_{pol}) = \begin{cases} g_{axis} + (g_{sep} - g_{axis})\rho_{pol}^2, & 0 \le \rho_{pol} \le 1 \\ g_{min} + (g_{sep} - g_{min})e^{-(\rho_{pol}-1)/D}, & 1 \le \rho_{pol} \le \rho_{max} \end{cases} \tag{13}$$

where g_{axis} is the on axis value, g_{sep} is the value at the separatrix, g_{min} is the minimum allowed value and D is the decay length parameter.

To include the gradients in the temperature and density adjacent to the separatrix in the dielectric tensor, we extend the plasma domain up to ρ_{max} (i.e. beyond the separatrix). Outside the plasma domain boundary, we apply the SOL dielectric tensor given by Eq. (8).

The gradients in the temperature and density adjacent to the flux surface $\rho_{pol} = 1$ occur in a narrow region that is only a couple of centimeters thick. To resolve this region and obtain a converged solution, a fine mesh is required. Instead of just increasing the mesh density isotropically using unstructured triangular elements (which would be computationally expensive), we propose using a boundary layer mesh instead. This technique uses high aspect ratio rectangular elements that mainly increases spatial resolution in the ρ_{pol} direction (see Fig. 5).

4. FEMIC simulation results for ITER

The effects of poloidal phasing of the ITER antennas were studied for a plasma with 46% deuterium, 46% tritium and 4% ^{3}He. In this scenario power is absorbed by fundamental ^{3}He and second harmonic tritium; deuterium absorption on the high field side is negligible. The main parameters are summarized in Table 1. No Neutral Beam Injection (NBI) was considered, impurities were neglected and only the dominant toroidal mode was considered. A vacuum model was employed in the SOL.

The numerical equilibrium used here originates from an ITER simulation, which is described in [30]. The shape of the equilibrium is important for the coupling between the antenna and the plasma. To ensure that all poloidal antenna straps have similar coupling to the plasma, the equilibrium was shifted 15 cm vertically and -2 cm horizontally and rescaled 2% vertically and -4% horizontally. To compensate for the shifting and rescaling, the position of the magnetic axis was moved -18 cm vertically.

Table 1. Parameters for ITER simulation. Here T and n refers to temperature and density respectively, and D is the decay length parameter.

Plasma species	DT with He-3 minority
Minority concentration	4%
B_0	5.3 T
Frequency	53 MHz
ρ_{max}	1.02
n_Φ	61
$T_{i,axis}$	24 keV
$T_{i,sep}$	2 keV
$T_{i,min}$	1 keV
$T_{e,axis}$	18 keV
$T_{e,sep}$	1.5 keV
$T_{e,min}$	0.75 keV
$n_{e,axis}$	8.0e19
$n_{e,sep}$	4.8e19
$n_{e,min}$	1.6e18
D	0.017
Triangular elements	378,132
Quadrilateral elements	106,120

The effect of poloidal phasing on the total coupled power is shown in Fig. 6. Here, the black solid line is the total coupled power using $B_0 = 5.3\,T$, which shows that low $\Delta\theta_{pol}$ provides more power to the plasma per unit current density squared compared with high $\Delta\theta_{pol}$. As a result of the asymmetry, the maximum and minimum coupling occurs at $\Delta\theta_{pol} = -28°$ and $\Delta\theta_{pol} = 152°$, respectively. The decrease in coupled power from maximum to minimum is 20%. The results also show that the coupling for $\Delta\theta_{pol} = -90°$ is slightly better than $\Delta\theta_{pol} = 90°$, where the decrease in coupled power from maximum is 5% and 15%, respectively. The absorbed power for the individual species follow a similar trend, i.e. the power partition is not sensitive to the poloidal phasing.

The coupling for the reversed magnetic field (i.e. $B_0 = -5.3\ T$) is illustrated by the black dashed line in Fig. 6. The results are similar to the one shown by the black solid line, but are mirrored around $\Delta\theta_{pol} = 0°$, an effect caused by the plasma gyrotropy.

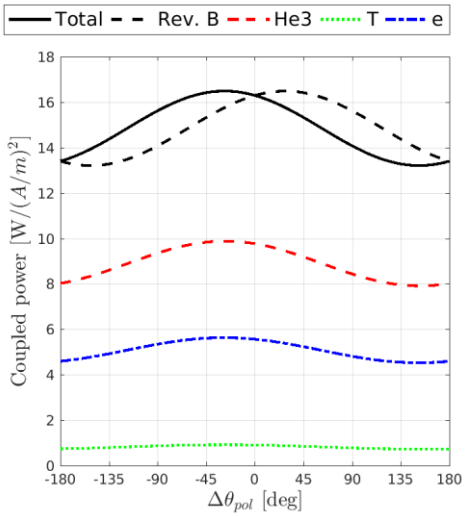

Fig 6: Coupled power per unit current density squared as a function of poloidal phase difference. The black solid and black dashed lines correspond to B_0 = 5.3T and B_0 =-5.3 T, respectively. The coupling to the individual species is illustrated by the colored curves and correspond to the case with B_0 = 5.3 T.

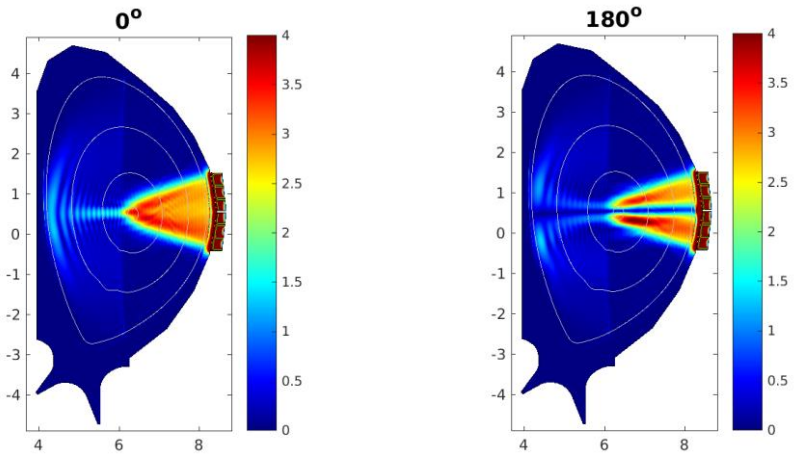

Fig 7. Norm of the right handed polarized wave component $\mathbf{E}_-$*. Left:* $\Delta\theta_{pol} = 0°$*, Right:* $\Delta\theta_{pol} = 180°$*. Color range is saturated at the antenna. Unit of the colorbars is [V/m] and axes in [m].*

In Fig. 7, we compare the right handed polarized wave component $\mathbf{E}_-$ for $\Delta\theta_{pol} = 0°$ and $\Delta\theta_{pol} = 180°$. For $\Delta\theta_{pol} = 0°$ the effect of destructive interference is close to its minimum; the launched wave forms one radiation lobe that is focused towards the magnetic axis. In contrast, for $\Delta\theta_{pol} = 180°$ two radiation lobes have formed with a destructive interference path in between that intersects the magnetic axis. The total power absorption for these two cases are shown in Fig. 8. For $\Delta\theta_{pol} = 0°$ the power is absorbed mainly by ions near the magnetic axis. For $\Delta\theta_{pol} = 180°$ two regions of ion absorption are formed, one above and one below the magnetic axis, which is a consequence of destructive interference of the wave occurring at the magnetic axis.

In Fig. 9, the $\mathbf{E}_-$ components for $\Delta\theta_{pol} = \pm 90°$ are presented. In both cases the destructive interference is clearly visible, where the strength of the interference is stronger for $\Delta\theta_{pol} =$

90°. The interference path is different for the two cases. Here, the interference path intersects the magnetic axis for $\Delta\theta_{pol} = 90°$, while for $\Delta\theta_{pol} = -90°$ the interference path passes just above the magnetic axis.

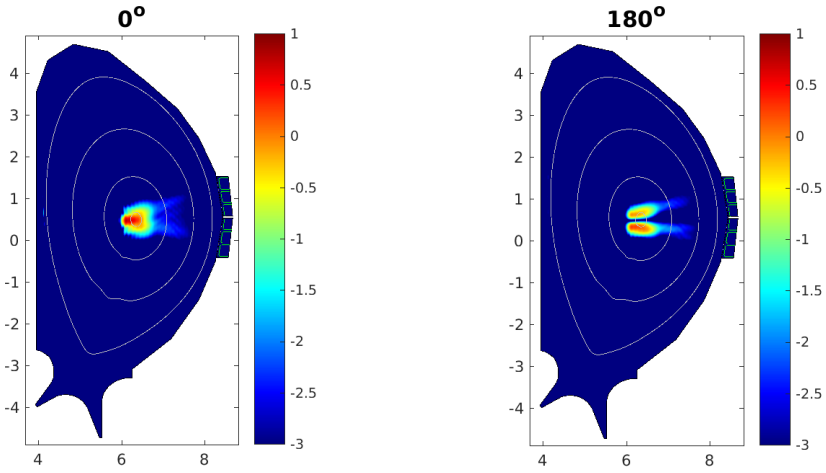

Fig. 8. Total power absorption $[W/m^3]$ in log scale. Left: $\Delta\theta_{pol} = 0^o$, Right: $\Delta\theta_{pol} = 180°^o$. Unit of the axes is in [m].

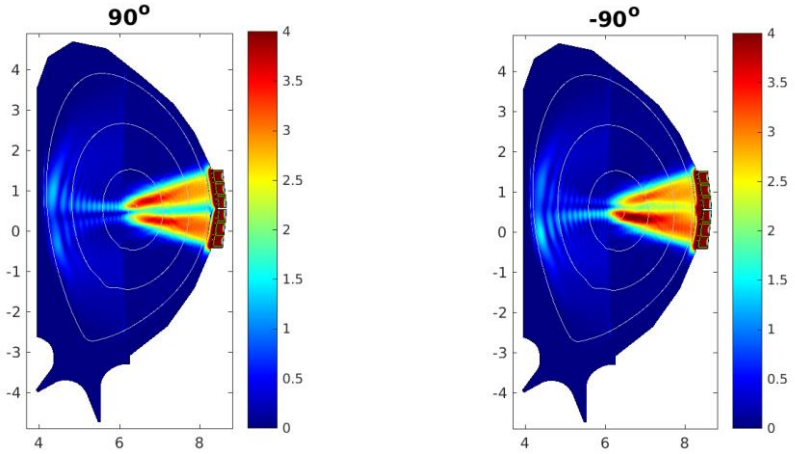

Fig 9: Norm of the right handed polarized wave component **E**_. *Left: $\Delta\theta_{pol} = 90°$, Right: $\Delta\theta_{pol} = -90°$. Color range is saturated at the antenna. Unit of the colorbars is [V/m] and axes in [m].*

The poloidal mode spectrum at the flux surface $\rho_{pol} = 0.5$ is shown in Fig. 10. Here, the poloidal modes are defined as $C_m e^{-im\theta}$, where $\theta = 2\pi \int dl / \oint dl$ is oriented clockwise around the ϕ axis and l is a poloidal line segment. These results show that the spectrum is slightly shifted towards the negative end. The dominant poloidal mode for $\Delta\theta_{pol} = 0°$ is $m = -1$. The dominant modes for $\Delta\theta_{pol} = 90°$ and $\Delta\theta_{pol} = -90°$ are $m = -3$ and $m = 1$, respectively. Note that both these two cases have a secondary peak located at $m = 5$ and $m = 7$, respectively. Finally, the case with $\Delta\theta_{pol} = 180°$ have two dominant poloidal modes at $m = -5$ and $m = 3$ and the mode at $m = -1$ has almost vanished.

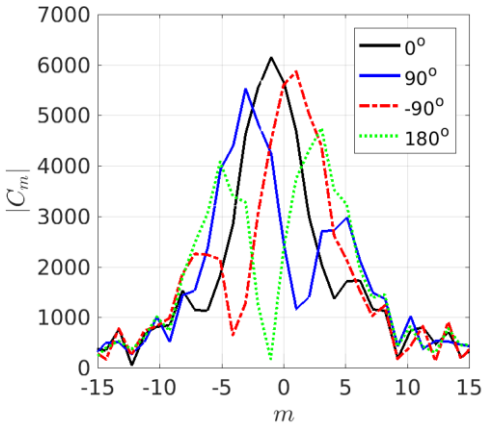

Fig 10. Poloidal mode spectra for different poloidal phasings of the ITER antenna at $\rho_{pol} = 0.5$. Here, m is the poloidal mode number.

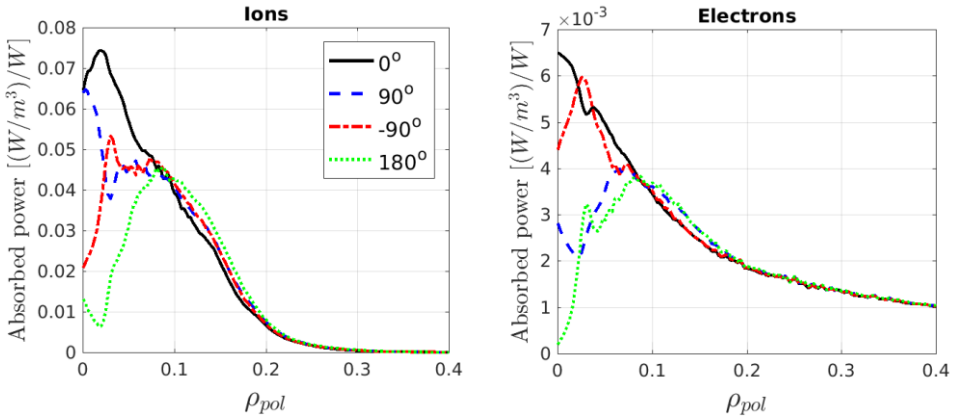

Fig 11: Flux surface averaged absorbed power for different poloidal phasings. Total launched ICRH power is 1 W. Left: ions, Right: electrons.

Fig. 11 shows the normalized absorbed power by ions (^{3}He and tritium) and electrons (total absorbed power is normalized to 1 W). In both cases, the effect of the poloidal phasing is localized to within $\rho_{pol} < 0.2$, were the strongest variations occur within $\rho_{pol} < 0.1$. The case with $\Delta\theta_{pol} = 0°$ provides the best on-axis absorption. In contrast, the case with $\Delta\theta_{pol} = 180°$ has the lowest on axis absorption and the power is instead deposited within $0.1 < \rho_{pol} < 0.2$.

5. FEMIC simulation results for JET-ILA

The study of the JET-ILA was performed for a deuterium plasma with 4% hydrogen using fundamental hydrogen minority and second harmonic deuterium heating near the magnetic axis. The main parameters are summarized in Table 2. No NBI was considered and impurities were neglected. We assumed that $T_i = T_e$ and considered the dominant toroidal mode number only. A vacuum was assumed in the SOL.

The magnetic equilibrium used in these simulations resemble a baseline scenario, where the last closed flux surface has been aligned with the ILA. A few flux surfaces are indicated in Fig. 13. The position of the magnetic axis was chosen so that the destructive interference path intersects it for $\Delta\theta_{pol} = 180°$.

The effect of poloidal phasing on the coupled power is shown in Fig. 12 (note that the ILA cannot operate at a higher poloidal phase than 90°, higher poloidal phases are hypothetical only). High coupling is achieved for low poloidal phase difference. As in the ITER case, the

coupling is not symmetric around $\Delta\theta_{pol} = 0°$. The maximum and minimum coupled powers occur for $\Delta\theta_{pol} = -15°$ and $\Delta\theta_{pol} = 165°$, respectively, where the decrease in total power is 32%. I.e. the asymmetry is weaker but the total power drop is higher in the JET-ILA compared with ITER. Furthermore, the coupling for $\Delta\theta_{pol} = -90°$ is higher than $\Delta\theta_{pol} = 90°$, where the drop from maximum is 12% and 20%, respectively. Since the coupled power for the individual species follows a similar trend, the power partition is not sensitive to the poloidal phasing.

Table 2: Input parameters for JET simulation. Here T and n refers to temperature and density respectively. D is the decay length.

Plasma species	D with 4% H
B_0	3.2 T
R_0	3 m
Frequency	49 MHz
ρ_{max}	1.05
n_ϕ	27
T_{axis}	10 keV
T_{sep}	3 keV
T_{min}	0.5 keV
$n_{e,axis}$	8.0e19
$n_{e,sep}$	4.8e19
$n_{e,min}$	1.6e18
D	0.008
Triangular elements	141371
Quadrilateral elements	69600

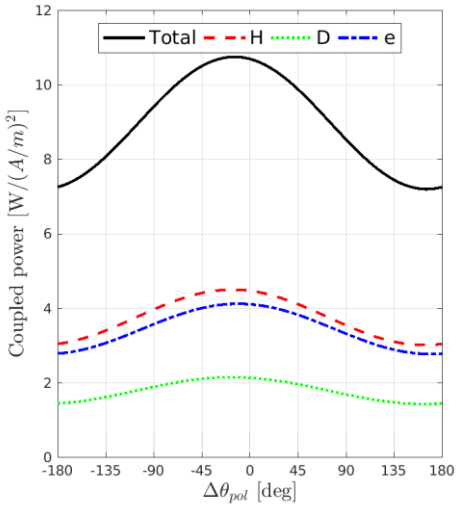

Fig 12: Coupled power per unit current density squared as a function of poloidal phase difference.

Fig. 13 shows the $\mathbf{E}_-$ component for $\Delta\theta_{pol} = 0°$ and $\Delta\theta_{pol} = 180°$. For $\Delta\theta_{pol} = 0°$, no destructive interference is observed and the ILA forms one radiation lobe focused towards the magnetic axis. For $\Delta\theta_{pol} = 180°$, two radiation lobes are formed. The destructive interference path in between intersects the magnetic axis, affecting the power deposition profile of both ions and electrons.

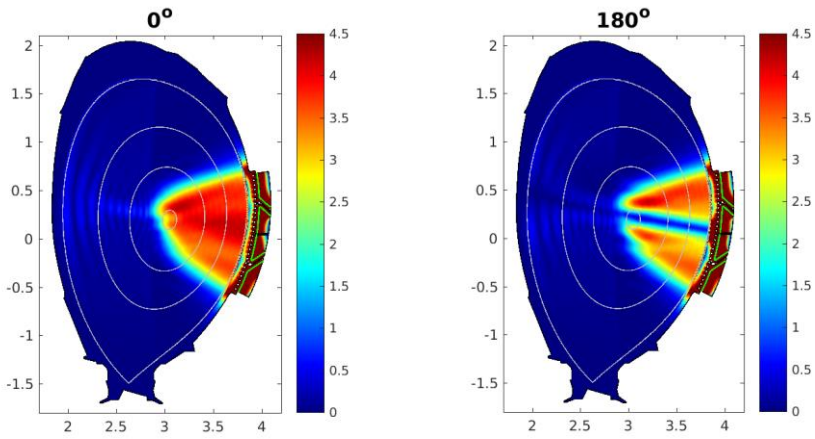

Fig 13. Norm of the right handed polarized wave component **E**-. *Left:* $\Delta\theta_{pol} = 0^o$, *Right:* $\Delta\theta_{pol} = 180°$. *Color is saturated at the antenna. Unit of the colorbars is [V/m] and axes in [m].*

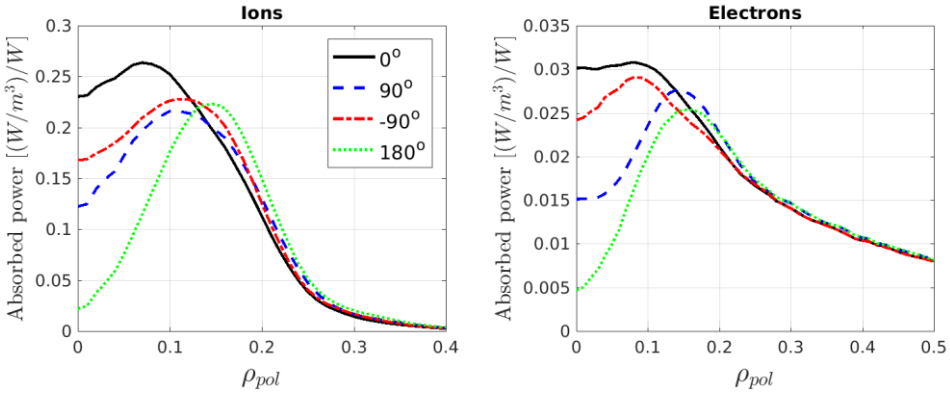

Fig 14: Flux surface averaged absorbed power for different poloidal phasings. Total launched ICRH power is 1 W. Left: ions, Right: electrons.

Fig. 14 shows the normalized absorbed power for ions and electrons. For both ions and electrons the effect of poloidal phasing occurs mainly within $\rho_{pol} < 0.25$, were the strongest variations occurs within $\rho_{pol} < 0.15$. The strongest and weakest on-axis absorption are obtained for $\Delta\theta_{pol} = 0°$ and $\Delta\theta_{pol} = 180°$, respectively. The absorption for the cases with $\Delta\theta_{pol} = \pm 90°$ is between the two extreme cases, where the poloidal phase $\Delta\theta_{pol} = -90°$ has slightly better on-axis absorption.

6. Discussion

The coupled power from the ICRH antennas to the plasma for both ITER and JET-ILA depends on the poloidal phase difference $\Delta\theta_{pol}$. In general, the coupled power decreases with increasing poloidal phase difference. This is a result of increasing destructive interference with increasing $\Delta\theta_{pol}$. The destructive interference is most clearly seen for scenarios with strong single pass damping. This is illustrated in Fig. 7 for ITER and Fig. 13 for JET-ILA. The cases with $\Delta\theta_{pol} = 0°$ have no degradation in performance due to destructive interference. However, tuning the ICRH antennas to $\Delta\theta_{pol} = 180°$, a destructive interference path is created near the equatorial plane, which reduces the coupled power. Fig. 8 shows the power absorption for $\Delta\theta_{pol} = 0°$ and $\Delta\theta_{pol} = 180°$ on ITER. Good on-axis absorption is obtained for $\Delta\theta_{pol} = 0°$, while for $\Delta\theta_{pol} = 180°$ the destructive interference forms two regions of power absorption, one above and one below the magnetic axis.

The coupled power is asymmetric around $\Delta\theta_{pol} = 0°$, as illustrated by Fig. 6 and Fig. 12. On ITER for $B_0 = 5.3\ T$, the maximum coupled power is obtained at $\Delta\theta_{pol} = -28°$, which is consistent with the results in [8]. A consequence of this result is that the performance in coupling for $\Delta\theta_{pol} = -90°$ is comparable with $\Delta\theta_{pol} = 0°$. Another interesting remark is that coupling is approximately 10% higher for $\Delta\theta_{pol} = -90°$ compared with $\Delta\theta_{pol} = 90°$. In fact, the performance of $\Delta\theta_{pol} = 90°$ is comparable with $\Delta\theta_{pol} = 180°$. At JET the coupling is more sensitive to the poloidal phasing, while the asymmetry is weaker (maximum coupling occurs at $\Delta\theta_{pol} = -15°$). Hence, the coupling for $\Delta\theta_{pol} = -90°$ is comparable to $\Delta\theta_{pol} = 90°$.

The asymmetry observed in the coupling on both ITER and JET is caused by the plasma gyrotropy [8,31,32]. This can be confirmed by reversing the sign of the magnetic field (i.e. $B_0 = -5.3\ T$), which mirrors the asymmetry in the coupled power (see Fig. 6). As a result, for $B_0 = 5.3\ T$ poloidal modes with negative mode number m (or modes with positive k_z) has better coupling to the plasma. This is illustrated in Fig. 10 where the poloidal mode spectrum is shifted towards negative poloidal mode numbers. Analysis using FEMIC reveals that the asymmetry in the coupling is not sensitive to the electron density or the temperature. Instead, we found that the asymmetry correlates with the cyclotron frequencies of the majority species and the wave frequency, i.e. $K_{xy}/K_{xx} \sim \omega_c/\omega$. On ITER, which will only be able to operate at $\Delta\theta_{pol} = \pm 90°$, one of these poloidal phasings will have higher coupling, which will ultimately depend on the orientation of the magnetic field.

Fig. 6 and Fig. 12 also show that the power absorbed by the individual species follow the same trend as the total coupled power. Hence, the power partition does not depend on $\Delta\theta_{pol}$. This also implies that the current drive per MW of ICRH power is also independent of $\Delta\theta_{pol}$. This was verified with FEMIC using an analytical model for the current drive based on [33].

Poloidal phasing does have an effect on the flux surface averaged power absorption. This is most clearly seen for on-axis heating, when the wake in the field strength due to destructive interference passes through the magnetic axis. On ITER, the normalized absorption on both ions and electrons inside $\rho_{pol} < 0.1$ decreases with increasing $\Delta\theta_{pol}$, as illustrated by Fig. 11. For $\Delta\theta_{pol} = 0°$, the absorption is peaked near the magnetic axis, while for $\Delta\theta_{pol} = 180°$ deposition profile is hollow. The power is instead deposited between $0.1 < \rho_{pol} < 0.2$. The absorption for the cases with $\Delta\theta = \pm 90°$ falls in between the two extreme cases.

On JET, the effect of poloidal phasing on the normalized absorbed power is similar to ITER (shown in Fig. 14). The case with $\Delta\theta = 0°$ has the highest on-axis absorption. By increasing $\Delta\theta_{pol}$, the hollowness in the normalized absorption profiles increases. This effect is localized to within $\rho_{pol} < 0.25$.

In this study, the FEMIC code was used to simulate the effect of poloidal phasing on ITER and JET. In comparison with other global wave solvers, one of the main advantages of the FEMIC code is the ability to have a detailed geometric representation in the poloidal plane of the plasma shape, SOL and antenna. The code can include arbitrary numbers of poloidal antenna straps with different current boundary conditions (which enables studies of poloidal phasing). Since FEMIC is based on FEM only, calculation times are typically fast. The ITER simulations in this study had approximately 4 million degrees of freedom. To solve the problem required around 25 GB of RAM and took approximately 8 minutes to calculate using a workstation equipped with two Intel Xeon E5-2687W processors (including the dielectric tensor calculations and basic post-processing). Another useful feature is the ability to control and apply advanced meshes to the geometry (through the LiveLink™ for MATLAB®). The boundary layer mesh feature is particularly useful in order to resolve gradients adjacent to the separatrix (i.e. pedestal region). This feature applies structured high aspect ratio rectangle

elements, allowing high resolution in a particular direction to a reasonable computational cost. This will enable detail calculations and studies of coupling and wave propagation in the SOL and pedestal regions.

In the present version of the FEMIC code, poloidal magnetic field is not considered. The poloidal field tends to cause a bending of the wave front inside the plasma, an effect that is not considered here. Another important effect of the poloidal field is that it causes a spatial dispersion effect in the parallel direction, i.e. the up- and downshift in the parallel wave vector. For the chosen scenarios, this effect is expected to be a small correction to the solution because of the high toroidal mode number chosen in the simulation and the strong single pass damping. However, the up- and downshift is more important for lower toroidal mode numbers of the coupled wave spectrum. The poloidal phasing may therefore affect the power deposition, partition and current drive efficiency for low toroidal mode numbers.

Finally, another remark that deserves attention is the FLR effect. For the fast wave the FLR effects is usually small. The quasi-homogeneous approximation to the dielectric tensor using the fast wave dispersion relation allows the inclusion of FLR effects and ion and electron damping for the fast wave only. If other waves are excited (e.g. slow wave), the dielectric response will not be treated correctly since FLR effects depends on the perpendicular wave number which differ for different waves.

7. Conclusions

Poloidal phasing of ICRH antennas creates an interference pattern in the regions where the radiation lobes of individual straps overlap. For the ITER antennas and JET-ILA a destructive interference pattern is formed near the equatorial plane that affects the coupling, the deposition profiles and the poloidal mode spectrum.

The coupled power is dependent on poloidal phase difference, $\Delta\theta_{pol}$, where the coupled power decreases with increasing $\Delta\theta_{pol}$. This is caused by destructive interference of the wave fields, which increases with $\Delta\theta_{pol}$. On both ITER and JET-ILA, the coupling is asymmetric around $\Delta\theta_{pol} = 0°$, due to the plasma gyrotropy. For a DT plasma on ITER and a D plasma on JET, the maximum coupled power to the plasma occurs at $\Delta\theta_{pol} = -28°$ and $\Delta\theta_{pol} = -15°$, respectively. For ITER, which will only be able to operate at $\Delta\theta_{pol} = \pm 90°$, the asymmetry for positive B_0 will favor $\Delta\theta_{pol} = -90°$ due to higher coupled power compared with $\Delta\theta_{pol} = 90°$. However, reversing the toroidal magnetic field will favor the other poloidal phasing scheme of $\Delta\theta_{pol} = 90°$.

The poloidal phasing did not have any significant effect on the power partition and current drive efficiency. However, it did affect the normalized flux surface averaged absorption profiles. For $\Delta\theta_{pol} = 0°$, the deposition profiles are peaked near the magnetic axis. With increasing poloidal phase difference, the on-axis absorption decrease and the profile becomes hollow at the plasma core. The effect of poloidal phasing on the absorption profiles is localized to the plasma core, which occurs within $\rho_{pol} < 0.2$ for ITER and $\rho_{pol} < 0.25$ for JET.

Acknowledgements

The authors are thankful for the fruitful discussions and help from D. Van Eester, E. Lerche and P. Dumortier. We thank our colleagues A. Weckmann and R. Fridström at KTH for interesting discussions and their comments on the manuscript. We also thank the student E. Gåvermark for his work on current drive using the FEMIC code.

This work has been carried out within the framework of the EUROfusion Consortium and has received funding from the European Union's Horizon 2020 research and innovation

program under grant agreement number 633053. The views and opinions expressed herein do not necessarily reflect those of the European Commission.

References

[1] ITER Physics Expert Group on Energetic Particles, Heating and Current Drive and ITER Physics Basis Editors 1999 *Nucl. Fusion* **39** 2495
[2] C. Gormezano *et al* 2007 *Nucl. Fusion* **47** S285
[3] J.R. Wilson *et al*, Physics of Plasmas **22**, 021801 (2015)
[4] P.U. Lamalle *et al*, AIP Conf. Proc **1187**, 265 (2009)
[5] L.-G. Eriksson *et al* 1999 *Nucl. Fusion* **39** 337
[6] P. Dumortier *et al* AIP Conference Proceedings **694**, 94 (2003)
[7] A. Messiaen *et al* 2009 *Nucl. Fusion* **49** 055004
[8] A. Messiaen *et al* 2010 *Nucl. Fusion* **50** 025026
[9] A. Messiaen and R. Weynants 2011, *Plasma Phys. Control. Fusion **53*** 085020
[10] T. Hellsten *et al* 2005 *Nucl. Fusion* **45** 706
[11] D. Van Eester, F. Louche, R. Koch, Nucl. Fusion 42, (2002) 310-328
[12] N.J. Fisch 1981 *Nucl. Fusion* **21** 15
[13] T. Hellsten *et al*, Phys. Rev. Lett. **74**, 3612 (1995)
[14] V. Lancellotti *et al* 2006 *Nucl. Fusion* **46** S476
[15] F Durodie et al 2012 *Plasma Phys. Control. Fusion* **54** 074012
[16] D.G. Swanson, Plasma waves 2nd edition, IOP Publishing Ltd (2003)
[17] T.H. Stix, Waves in plasmas, AIP, New York (1992)
[18] N. Bertelli et al, AIP Conference Proceedings **1689**, 030010 (2015)
[19] E. Lerche et al, J. Nucl. Mater., **463** (2015) 634-639
[20] M. Brambilla and R. Bilato 2006 *Nucl. Fusion* **46** S387
[21] R. Dumont 2009 *Nucl. Fusion* **49** 075033
[22] – P.U. Lamalle, PhD thesis – Université de Mons (1994) LPP-ERM/KMS Laboratory Report 101
[23] P. Popovich, W.A: Cooper, L. Villard, Comput. Phys. Comm. 175 (2006) 250-263
[24] N. Mellet et al, Comput. Phys. Comm. 182 (2011) 570-589
[25] L. Villard, S. Brunner, and J. Vaclavik 1995 *Nucl. Fusion* **35** 1173
[26] E.F. Jaeger et al, Physics of Plasmas **9**, 1873 (2002)
[27] S. Shiraiwa *et al* 2017 *Nucl. Fusion* **57** 086048
[28] URL: www.mathworks.com
[29] URL: www.comsol.com
[30] L. Figini et al, EPJ Web of Conferences **32**, 01001 (2012)
[31] J. Jaeger *et al*, AIP Conf. Proc. **403**, 285 (1997)
[32] E.F. Jaeger *et al* 1998 *Nucl. Fusion* **38** 1
[33] D.A. Ehst and C.F.F. Karney 1991 *Nucl. Fusion* **31** 1933